The Astrophysical Journal, 694:1266–1280, 2009 April 1 doi:10.1088/0004-637X/694/2/1266

SPITZER OBSERVATIONS OF MOLECULAR HYDROGEN IN INTERACTING SUPERNOVA REMNANTS

John W. Hewitt[1], Jeonghee Rho[2], Morten Andersen[2], and William T. Reach[2]
[1] Department of Physics and Astronomy, Northwestern University, Evanston, IL 60208, USA
[2] Spitzer Science Center, California Institute of Technology, Pasadena, CA 91125, USA
Received 2008 November 15; accepted 2009 January 5; published 2009 March 24

ABSTRACT

With *Spitzer* IRS, we have obtained sensitive low-resolution spectroscopy from 5 to 35 μm for six supernova remnants (SNRs) that show evidence of shocked molecular gas: Kes 69, 3C 396, Kes 17, G346.6−0.2, G348.5−0.0, and G349.7+0.2. Bright pure rotational lines of molecular hydrogen are detected at the shock front in all remnants, indicative of radiative cooling from shocks interacting with dense clouds. We find the excitation of H_2 S(0)–S(7) lines in these SNRs requires two nondissociative shock components: a slow 10 km s^{-1} C-shock through clumps of density 10^6 cm^{-3}, and a faster 40–70 km s^{-1} C-shock through a medium of density 10^4 cm^{-3}. The ortho-to-para ratio for H_2 in the warm shocked gas is typically found to be much less than the LTE value, suggesting that these SNRs are propagating into cold quiescent clouds. Additionally, a total of 13 atomic fine-structure transitions of Ar^+, Ar^{++}, Fe^+, Ne^+, Ne^{++}, S^{++}, and Si^+ are detected. The ionic emitting regions are spatially segregated from the molecular emitting regions within the IRS slits. The presence of ionic lines with high appearance potential requires the presence of much faster, dissociative shocks through a lower density medium. The IRS slits are sufficiently wide to include regions outside the SNR which permits emission from diffuse gas around the remnants to be separated from the shocked emission. We find the diffuse H_2 gas projected outside the SNR is excited to a temperature of 100–300 K with a warm gas fraction of at least 0.5%–15% along the line of sight.

Key words: infrared: ISM – supernova remnants – shock waves – ISM: clouds – ISM: lines and bands – ISM: molecules

Online-only material: color figures

1. INTRODUCTION

As a supernova remnant evolves into its surrounding environment, it becomes the dominant reservoir of energy that drives dynamics and chemistry in the interstellar medium (McKee & Ostriker 1977). As massive stars in general do not drift far from their parent cloud in their short lifetimes, supernovae near giant molecular clouds (MCs) should be common. Yet there are only a handful of supernova remnants (SNRs) which have been clearly identified as interacting with MCs. Pure rotational transitions of molecular hydrogen (H_2) are excellent indicators of such interactions as high columns of H_2 can survive the passage of the shock.

Molecular hydrogen is the most abundant molecule in the Universe, playing a crucial role in the interstellar medium (ISM) as a catalyst of chemistry and a major coolant. H_2 is excited by energetic processes such as shocks and photodissociation regions, with numerous bright emission lines in the near- and mid-infrared (IR) available as detailed diagnostics of the excited gas. The low-lying pure rotational transitions of H_2 probe the bulk of the gas involved in the shock interaction and are excellent diagnostics of the shock conditions. Due to their relatively low critical densities, the S(0)–S(7) transitions are not good diagnostics of the excitation mechanism; however, supernova remnant shocks have the advantage of being comparatively simple systems to understand detailed shock processes as there is no complicating stellar radiation source. Galactic supernova remnants are an important template for other shock interactions, for example the spectacular galaxy-scale shocks seen in Stephan's Quintet (Appleton et al. 2006).

In this paper, we report the results of mid-IR long-slit spectroscopy of six SNRs identified as bright in molecular lines. These SNRs have not been previously studied in the mid-IR and represent a diversification of the common sample of nearby interacting SNRs such as IC 443, W28, W44 (see Rho et al. 2001; Neufeld et al. 2007 and references therein). The observations are briefly described in Section 2, followed by a summary of the properties and observed line emission for each source in Section 3. Section 3.3 pertains to the physical conditions of the detected pure rotational H_2 lines. Sections 4.1 and 4.2 reconcile the observed molecular and atomic lines, respectively. Section 5 presents a discussion of diffuse H_2 observed outside the shock front.

2. OBSERVATIONS

Motivated by the detection of eighteen IR-bright SNRs using the GLIMPSE survey (Reach et al. 2006), we have selected six SNRs which display *Spitzer* Infrared Array Camera (IRAC) colors indicative of molecular shocks. Of the six interacting remnants we consider in this work, four SNRs—Kes 69, G346.6−0.2, G348.5−0.0, and G349.7+0.2—have previously identified OH(1720 MHz) masers which have been established as excellent signposts of interaction with an adjacent MC (Yusef-Zadeh et al. 2003). For Kes 17 and 3C 396, the evidence for interaction was less clear, but both have bright filamentary radio shells and IRAC band ratios indicative of molecular shocks (Reach et al. 2006).

The *Spitzer Space Telescope* Infrared Spectrograph (IRS) was used to obtain spectra of these SNRs to characterize the nature of emission using the short-low (SL, 5.2–15 μm) and long-low (LL, 14–42.4 μm) modules and with a resolving power of R $\approx$ 60–125. In each remnant, a single position coincident with a peak in the IRAC channel 2 emission was chosen (see Table 1). Exposure times of 150–180 s were used for the SL and LL modes. As the exposures were nodded, the effective

Table 1
Properties of Observed Supernova Remnants

Parameter	Kes 69	3C 396	Kes 17	G346.6−0.2	G348.5−0.0	G349.7+0.2
R.A. (J2000)	18:33:01.89	19:03:56.21	13:05:32.75	17:13:43.82	17:15:04.90	17:21:24.90
Decl. (J2000)	−10:13:44.2	+05:25:49.7	−62:40:06.0	−40:18:06.0	−38:33:41.0	−37:29:11.6
Diameter (′)	20	8 × 6	8	8	10	2.5
Distance (kpc)	5.2	⩾7	⩾9.7	11	13.7	22
Physical size (pc)	30	⩾16 × 12	⩾23	26	39	16
Velocity (km s^{-1})	+80, +69	?	?	−76	−22	+16
N_H (10^{22} cm^{-2})	2.4	4.7	3.6	2.68	2.8	5.8
τ(9.7)	0.95	1.8	1.4	1.05	1.1	2.3
A_V (mag)	13	25	19.3	14.3	15	31
References	1, 2	3, 4	5, 11	6, 7, 11	5, 10, 11	8, 9

References: (1) Wilson 1972; (2) Yusef-Zadeh et al. 2003; (3) Harrus & Slane 1999; (4) Olbert et al. 2003; (5) Caswell et al. 1975; (6) Dubner et al. 1993; (7) Koralesky et al. 1998; (8) Slane et al. 2002; (9) Lazendic et al. 2005; (10) Reynoso & Mangum 2000; (11) This work.

integration time for the overlapping region between both orders is doubled typically producing a line signal-to-noise ratio of 20. For G349.7+0.2, the remnant is bright enough that only half the integration time was needed. A cluster of reference sky positions devoid of IR sources were observed within a few degrees of the targets. Subtracting the median-averaged reference position from the source positions successfully mitigated most rogue pixels. The remaining rogue pixels were removed manually utilizing the IRS CLEAN program provided by the Spitzer Science Center. Additionally, the slits were nodded with respect to the target position so that different sections of the slit observed the same overlapping target position.

Spectra were extracted from the region of overlap between the IRS SL and LL slits and aperture correction was applied. We did not find it not necessary to defringe the observed spectra. For each target we subtracted a local background using a nearby position within the same IRS nodded pair. In all cases, a position which lies outside the remnant, and has the lowest background region from one of four co-added observations is used. As the short-low and long-low slits are aligned roughly perpendicular to each other, we must use different locations as representative local backgrounds for the short- and long-orders. In practice the backgrounds did not differ substantially and produced only minor discontinuities between the two IRS orders. The H_2 S(2)–S(7) lines are only detected from the SNR interaction regions and are not affected by a local background subtraction. However, the H_2 S(0) and S(1) lines show diffuse emission across the slit, even outside the SNR, but with a clear enhancement of emission at the SNR shell. The detailed properties of the remnant and diffuse background are discussed separately in Sections 3.3 and 5, respectively.

3. RESULTS

3.1. IRS Spectra and Line Brightnesses

IRS spectra of SNRs Kes 69, 3C 396, Kes 17, G346.6−0.2, G348.5−0.0, and G349.7+0.2 after local background subtraction are presented in Figure 1 with prominent emission lines and PAH features labeled. For all remnants, bright pure rotational transitions of H_2 (0,0) S(0)–S(7) are detected. Atomic sulfur and several ionized fine-structure transitions—Ar^+, Ar^{++}, Fe^+, Ne^+, Ne^{++}, S^{++}, and Si^+—are also observed. The multiple molecular and ionic transitions detected with *Spitzer* are the first clear evidence of interaction in most of these remnants. For 3C 396, there is evidence that molecular and ionic lines are spatially segregated within the IRS slits shown in Figures 2 and 3. A steadily rising background continuum level and in some cases PAH emission are also seen after local background subtraction, but detailed analysis and discussion of this emission is deferred to a future paper. In general, there is good agreement between the IRS spectra and the nature of IR emission predicted from the simple color template analysis of IRAC band emission by Reach et al. (2006).

Properties of the SNRs considered in this work are given in Table 1. The best distance determination is used to obtain a corresponding physical size of the remnants' radio shell. For Kes 69, 3C 396, and G349.2+0.2, we used extinction values from the literature. For Kes 17, G348.5−0.0, and G346.6−0.2, we computed the visual extinction in two or three methods listed below and found the most consistent values. First, the IRS spectra are fit by the lines and continuum (using PAHFIT; Smith et al. 2007) where the silicate absorption dips are important to determine the extinction. We have verified the extinction solutions of PAHFIT by estimating the depth of the 9.7 μm silicate feature against the continuum of the remnant. We used the extinction curve of Draine (2003) with a visible extinction parameter, $R_V = A_V/E(B-V)$, of 3.1 appropriate for the diffuse ISM in the Milky Way to derive the extinction from the 9.7 μm optical depth. Second, the total hydrogen column density along the line of sight is derived from X-ray observations for Kes 17 and G348.5−0.0 using archival *ASCA* data. The detailed X-ray analysis will be presented in a subsequent paper (J. Rho et al. 2009, in preparation). Third, we have used H I and CO data (Dickey & Lockman 1990; Dame et al. 2001) to estimate the total hydrogen column to the SNR. When the kinematics of the SNR are known from masers, we can estimate the column of atomic and molecular hydrogen by integrating up to the systemic velocity of the SNR. This gives an upper limit to the hydrogen column which is appropriate if the SNR is located at the far distance solution of the Galactic rotation curve. This was an important constraint for G348.5−0.0 as it is the only SNR without detected central X-ray emission or an associated pulsar, and it is believed to lie at the far distance near SNR CTB 37A. Given there is still some uncertainty in the appropriate de-reddening values for these SNRS, we list the observed line intensities after local background subtraction in Table 2; the values after extinction correction are given in Table 3.

Using the distance and extinction given in Table 1, the total luminosity of IR lines observed for Kes 69, 3C 396, Kes 17, G346.6−0.2, G348.5−0.0, and G349.7+0.2 are derived. In all

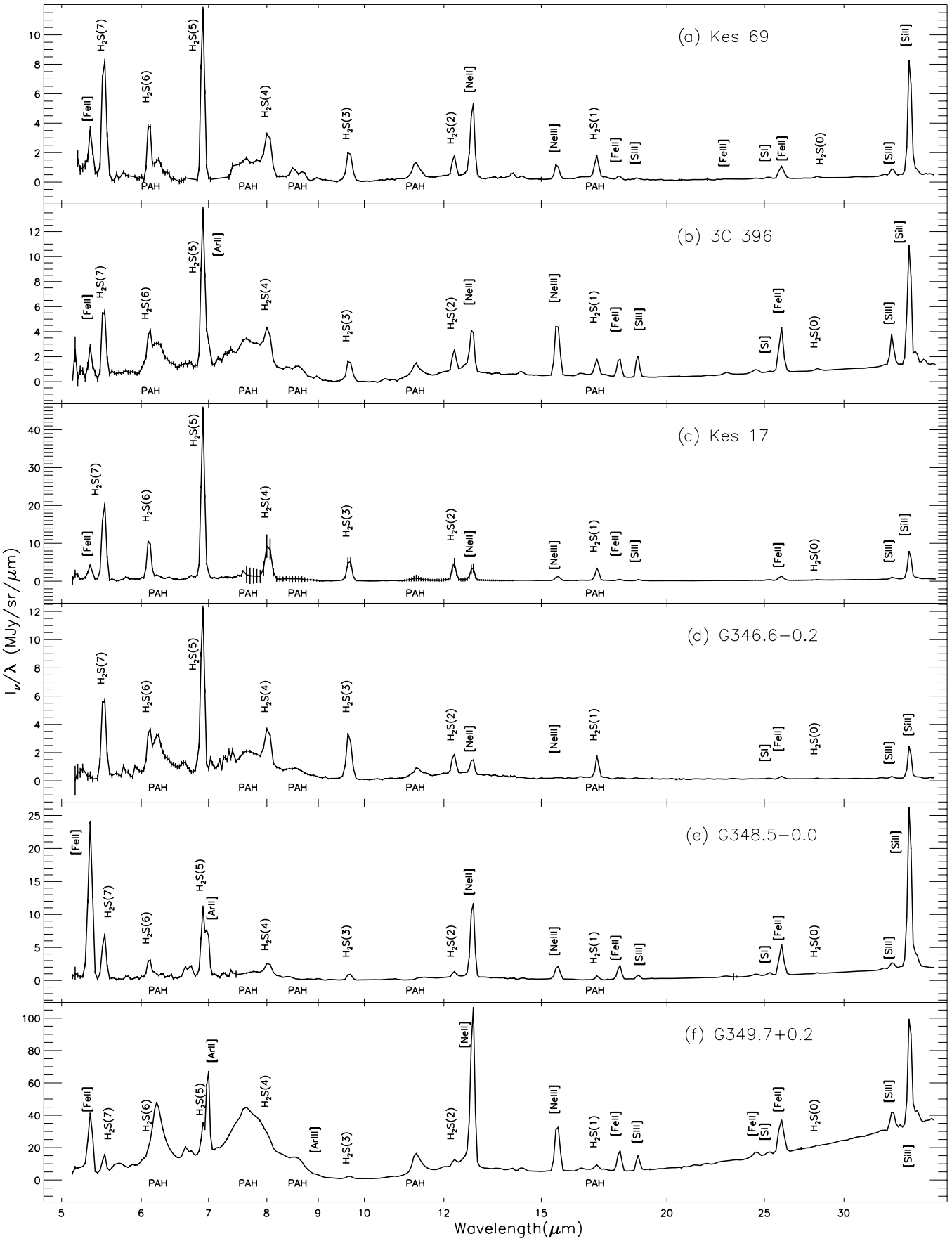

Figure 1. Observed IRS spectra after local background subtraction. Detected lines and PAH features are labeled. From top to bottom: (a) Kes 69, (b) 3C 396, (c) Kes 17, (d) G346.6−0.2, (e) G348.5−0.0, and (f) G349.7+0.2.

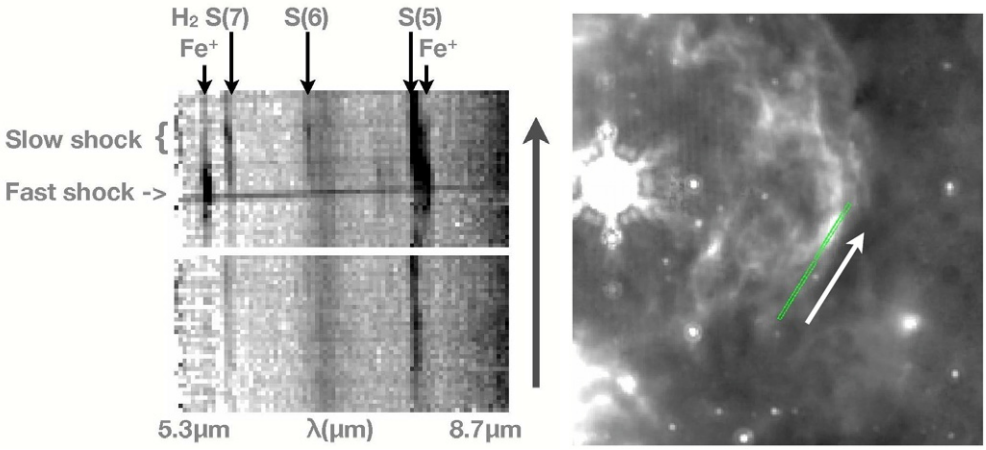

Figure 2. Left: spectral images for the short-low second order of IRS for 3C 396 between 5.1 and 8.7 μm. Right: MIPS 24 μm image of SNR 3C 396 with the IRS SL2 slit overlaid. An arrow is drawn to indicate the direction along the slit.

(A color version of this figure is available in the online journal.)

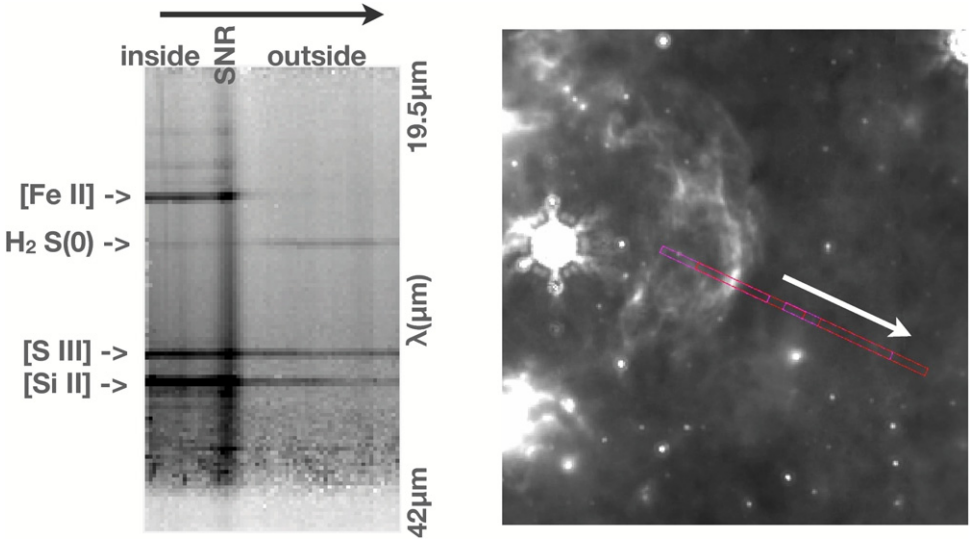

Figure 3. Left: spectral image for the long-low first order of IRS for 3C 396 between 19.5 and 42.4 μm. Note that the spectrum is severely degraded at wavelengths greater than 35 μm toward the bottom of the spectral image. Right: MIPS 24 μm image of SNR 3C 396 with the IRS LL1 slit overlaid. An arrow is drawn to indicate the direction along the slit.

(A color version of this figure is available in the online journal.)

cases, the lowest luminosity source was Kes 69 and the brightest was G349.7+0.2. For H_2 S(0)–S(7), we find a total luminosity of 1.4–68 $L_\odot$. For ionic lines with ionization potentials less than 13.6 eV (Fe^+, Si^+) and greater than 13.6 eV (Ar^+, Ar^{++}, Ne^+, Ne^{++}, and S^{++}), we find a total luminosity between 5–1212 and 0.8–595 $L_\odot$, respectively. These two groups of ions are considered separately because they require different physical conditions and previous spectral line mapping of interacting SNRs has shown the two are not spatially correlated (Neufeld et al. 2007). Line luminosities for each species are given in Table 4 for comparison. The [Si II] 34.8 μm line is always observed as a significant cooling line. For Kes 69, Kes 17, and G346.6−0.2, molecular hydrogen lines are also significant coolants in the observed IRS wavelengths. For 3C 396 and G348.5−0.0, the cooling from the three main ionic lines of Fe, Ne, and Si is comparable to the cooling from H_2 lines. The youngest remnant G349.7+0.2 has bright ionic lines that are far more luminous than H_2. We note that the luminosities given are for the observed apertures which vary with wavelength. For the IRS SL and LL modules, the apertures are $3.6'' \times 8''$ and $10.5'' \times 20''$, respectively.

3.2. Individual Supernova Remnants

Here, a brief description of the properties of each SNR is given, noting the existing evidence for interaction and the individual results of our *Spitzer* IRS observations.

G21.8−0.2 (Kes 69). The SNR Kes 69 has a clear southern radio shell but little radio emission to the north. IRAC 4.5 μm images that include emission from H_2 show a faint filament along the prominent southern radio shell. A single OH(1720 MHz) maser with a velocity of +69.1 km s^{-1} has been detected in the far northern extent of the remnant (Frail et al. 1996). Recent CO and H I observations show Kes 69 is at a distance of 5.2 kpc with a systemic velocity of +80 km s^{-1} (Tian & Leahy 2008; Zhou et al. 2009). Near this velocity OH(1720 MHz) emission

Table 2
Observed Brightness of Emission Lines after Local Background Subtraction

Transition	λ (μm)	Intensity (erg cm^{-2} s^{-1} sr^{-1})					
		Kes 69	3C 396	Kes 17	G346.6−0.2	G348.5−0.0	G349.7+0.2
H_2 S(0)	28.219	4.29(0.28)E-6	6.85(2.90)E-6	4.54(0.28)E-6	1.34(0.25)E-6	3.26(0.27)E-6	1.54(0.15)E-5
H_2 S(1)	17.035	4.14(0.03)E-5	3.15(0.41)E-5	1.00(0.01)E-4	4.26(0.05)E-5	1.27(0.04)E-5	8.18(0.10)E-5
H_2 S(2)	12.279	4.51(0.02)E-5	4.02(0.41)E-5	1.58(0.30)E-4	4.60(0.07)E-5	2.69(0.07)E-5	1.40(0.02)E-4
H_2 S(3)	9.665	8.44(0.24)E-5	2.56(0.19)E-5	2.20(0.24)E-4	1.32(0.02)E-4	2.89(0.11)E-5	6.89(0.17)E-5
H_2 S(4)	8.025	1.24(0.16)E-4	1.14(0.12)E-4	4.56(0.55)E-4	1.20(0.05)E-4	8.76(0.32)E-4	2.32(0.05)E-4
H_2 S(5)	6.910	2.03(0.10)E-4	3.29(0.21)E-4	1.28(0.09)E-3	3.64(0.19)E-4	2.99(0.04)E-4	4.61(0.07)E-4
H_2 S(6)	6.109	1.06(0.05)E-4	6.15(0.78)E-5	3.80(0.32)E-4	6.45(0.56)E-5	8.87(0.41)E-5	... [a]
H_2 S(7)	5.511	3.15(0.09)E-4	1.60(0.14)E-4	7.56(0.07)E-3	2.22(0.05)E-4	2.47(0.05)E-4	3.20(0.10)E-4
[Fe II]	5.35	1.27(0.01)E-4	2.82(0.11)E-4	1.55(0.07)E-4	...	8.55(0.07)E-4	1.49(0.02)E-3
[Ar II]	6.98	...	...	...	...	2.05(0.05)E-4	1.58(0.01)E-3
[Ar III]	9.00	...	...	...	...	...	2.35(0.41)E-5
[Ne II]	12.8	1.50(0.01)E-4	1.10(0.08)E-4	1.18(0.03)E-4	3.20(0.08)E-5	3.50(0.01)E-4	2.92(0.02)E-3
[Ne III]	15.5	3.72(0.24)E-5	1.51(0.08)E-4	4.43(0.02)E-5	2.47(0.28)E-6	7.42(0.03)E-5	1.11(0.01)E-3
[Fe II]	17.9	8.37(0.27)E-6	3.55(0.04)E-5	1.17(0.06)E-5	...	5.88(0.05)E-5	3.77(0.02)E-4
[S III]	18.7	4.19(0.26)E-6	3.65(0.03)E-5	8.83(0.34)E-6	1.62(0.26)E-6	1.59(0.03)E-5	2.43(0.03)E-4
[Fe II]	24.5	3.44(0.23)E-6	1.31(0.38)E-5	2.76(0.13)E-6	...	1.62(0.03)E-5	1.90(0.03)E-4
[S I]	25.2	5.64(0.29)E-6	...	7.94(0.25)E-6	1.95(0.30)E-6	1.77(0.02)E-5	1.17(0.02)E-4
[Fe II][b]	25.9	3.84(0.02)E-5	9.94(0.01)E-5	4.54(0.01)E-5	7.00(0.19)E-6	1.80(0.01)E-4	9.82(0.05)E-4
[S III]	33.5	1.52(0.04)E-5	5.58(0.09)E-5	1.94(0.03)E-5	3.45(0.30)E-6	3.35(0.03)E-5	4.02(0.03)E-4
[Si II]	34.8	2.53(0.01)E-4	2.12(0.05)E-4	2.30(0.01)E-4	6.93(0.05)E-5	7.14(0.02)E-4	2.12(0.02)E-3

Notes.
[a] Blended with strong PAH feature.
[b] Blended with [O IV] 25.9 μm line.

Table 3
De-Reddened Brightness of Emission Lines Assuming an Extinction Curve of $R_V = 3.1$

Transition	λ (μm)	Intensity (erg cm^{-2} s^{-1} sr^{-1})					
		Kes 69	3C 396	Kes 17	G346.6−0.2	G348.5−0.0	G349.7+0.2
H_2 S(0)	28.219	4.58(1.51)E-6	9.69(4.10)E-6	1.33(0.22)E-5	1.49(0.30)E-6	4.01(0.27)E-6	2.11(0.19)E-5
H_2 S(1)	17.035	5.50(0.06)E-5	5.70(0.75)E-5	1.98(0.13)E-4	6.01(0.16)E-5	1.81(0.44)E-5	1.88(0.39)E-4
H_2 S(2)	12.279	5.75(0.07)E-5	8.03(0.81)E-5	2.68(0.17)E-4	6.83(0.11)E-5	4.07(0.11)E-5	3.92(0.66)E-4
H_2 S(3)	9.665	1.45(0.08)E-4	1.47(0.11)E-4	9.09(0.50)E-4	3.44(0.38)E-4	8.18(0.30)E-5	5.40(0.17)E-4
H_2 S(4)	8.025	1.56(0.14)E-4	2.15(0.23)E-4	7.59(0.55)E-4	1.75(0.07)E-4	1.28(0.04)E-4	3.53(0.68)E-4
H_2 S(5)	6.910	3.49(0.28)E-4	4.61(0.30)E-4	1.71(0.09)E-3	3.58(0.86)E-4	3.66(0.05)E-4	5.19(1.06)E-4
H_2 S(6)	6.109	1.13(0.12)E-4	9.36(1.19)E-5	5.10(0.32)E-4	8.36(0.66)E-5	1.14(0.05)E-4	... [a]
H_2 S(7)	5.511	3.44(0.21)E-4	2.48(0.21)E-4	1.00(0.07)E-3	2.78(0.09)E-4	3.21(0.06)E-4	5.34(0.62)E-4
[Fe II]	5.35	1.61(0.10)E-4	4.47(0.07)E-4	2.22(0.10)E-4	...	1.13(0.02)E-3	2.50(0.02)E-3
[Ar II]	6.98	...	...	...	...	2.51(0.05)E-4	2.30(0.01)E-3
[Ar III]	9.00	...	...	...	...	...	1.19(0.20)E-4
[Ne II]	12.8	2.01(0.09)E-4	1.96(0.15)E-4	1.83(0.04)E-4	4.44(0.09)E-5	4.93(0.01)E-4	5.51(0.03)E-3
[Ne III]	15.5	4.74(0.04)E-5	2.43(0.13)E-4	6.37(0.03)E-5	3.24(0.36)E-6	9.84(0.04)E-5	1.88(0.01)E-3
[Fe II]	17.9	1.16(0.04)E-5	6.71(0.06)E-5	1.90(0.10)E-5	...	8.59(0.08)E-5	7.62(0.02)E-4
[S III]	18.7	5.79(0.36)E-6	6.88(0.05)E-5	1.44(0.06)E-5	2.33(0.38)E-6	2.32(0.04)E-5	4.90(0.03)E-4
[Fe II]	24.5	4.23(0.29)E-6	1.97(0.38)E-5	3.76(0.17)E-6	...	2.06(0.03)E-5	2.97(0.03)E-4
[S I]	25.2	6.88(0.36)E-6	...	1.07(0.03)E-5	2.44(0.32)E-6	2.23(0.03)E-5	1.80(0.02)E-4
[Fe II][b]	25.9	4.66(0.03)E-5	1.45(0.02)E-4	6.06(0.02)E-5	8.68(0.21)E-6	2.25(0.02)E-4	1.49(0.01)E-3
[S III]	33.5	1.76(0.05)E-5	7.42(0.19)E-5	2.41(0.03)E-5	4.06(0.30)E-6	3.97(0.04)E-5	5.50(0.04)E-4
[Si II]	34.8	2.90(0.04)E-4	2.76(0.07)E-4	2.82(0.01)E-4	8.06(0.05)E-5	8.36(0.03)E-4	2.84(0.04)E-3

Notes.
[a] Blended with strong PAH feature.
[b] Blended with [O IV] 25.9 μm line.

along the radio shell indicates a molecular shock (Hewitt et al. 2008). *ROSAT* observations give a column of $N_H = 2.4 \times 10^{22}$ cm^{-2} (Yusef-Zadeh et al. 2003).

G39.2−0.3 (3C 396). The 3C 396 has a bright radio shell and a central X-ray emission. The western shell appears brighter in both radio and X-ray emission, suggestive of interaction with an MC. IRAC images in all bands show a bright IR filament along the western edge with colors indicating an ionic or molecular shock. There is a compact central X-ray nebula with a photon index of 1.5 consistent with a central pulsar wind nebula (Olbert et al. 2003). There is also significant thermal X-ray emission from the interior of the SNR not related to the pulsar wind nebula (Harrus & Slane 1999). The total hydrogen column for the supernova remnant measured by both *Chandra* and *ASCA*

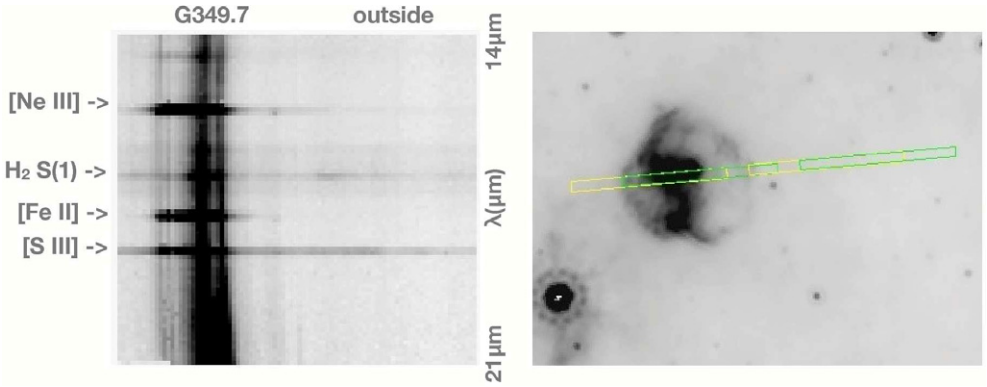

Figure 4. Left: spectral image of the long-low second order of IRS for G349.7+0.2 between 14 and 21 μm. Diffuse PAH emission can be seen around the H_2 S(1) line. Right: MIPS 24 μm image of SNR G349.7+0.2 with the IRS LL2 slit overlaid.

(A color version of this figure is available in the online journal.)

Table 4
Comparison of IR Line Luminosities

Luminosity ($L_\odot$)	Kes 69	3C 396	Kes 17	G346.6−0.2	G348.5−0.0	G349.7+0.2
H_2 S(0)–S(7)	1.4	2.5	21	7.2	6.8	68
H_2 S(0)–S(2)	0.5	0.9	6.3	2.2	1.5	37
H_2 S(5)–S(7)	0.6	0.9	8.2	2.3	3.9	13
Ar	...	...	...	...	1.4	36
Fe	0.7	3.8	3.2	0.4	26	448
Ne	0.6	2.6	2.3	0.4	9.5	358
S	0.3	2.4	1.5	0.3	4.9	201
Si	4.4	6.5	15	5.4	85	764

is 4.7 × 10^{22} cm^{-2} (Harrus & Slane 1999; Olbert et al. 2003). Assuming the SNR and pulsar wind nebula are related, a distance of 6.5 kpc is obtained from the hydrogen column.

The obtained spectrum of 3C 396 from the western IR filament shows a wealth of both H_2 and ionic lines of Ar, Fe, Ne, S, and Si. Figure 2 shows a clear spatial separation between the H_2 and ionic lines along the western shell. This is clear evidence for spatial variation of physical conditions along the shock front. In Figure 3, diffuse interstellar emission lines of H_2 S(0), [S III], and [Si II] are seen outside the SNR, whereas [Fe II] is only prominent inside the remnant. These long slit observations hold an advantage over spectral mapping of nearby remnants in that the emission associated with the SNR can be clearly distinguished from diffuse emission using local background subtraction.

G304.6+0.1 (Kes 17). An incomplete radio shell, Kes 17 has prominent IR filaments with colors indicating bright emission from shocked H_2 (Reach et al. 2006). The remnant is not well studied, but H I absorption suggests a distance of at least 9.7 kpc (Caswell et al. 1975). Given the absence of clear kinematic signatures, we give lower limits for the distance and size of Kes 17 in Table 1. Archival *ASCA* observations show diffuse interior X-ray emission, allowing us to derive a total hydrogen column of 3.6 × 10^{22} cm^{-2} toward Kes 17.

G346.6−0.2. This remnant has a faint radio shell filled with diffuse thermal X-ray emission, making it a mixed-morphology SNR. Five OH(1720 MHz) masers are detected along the southern shell of the SNR near a velocity of −76 km s^{-1}; Zeeman splitting of the maser line gives a line-of-sight magnetic field of +1.7 ± 0.1 mG (Koralesky et al. 1998). The kinematics implied by the velocity of the associated maser gives a near/far distance 5.5 or 11 kpc. Archival *ASCA* GIS observations show diffuse X-ray emission from the remnants interior which is best fit by a total hydrogen column of $2.68^{+2.32}_{-0.68}$ × 10^{22} cm^{-2} and a temperature of $kT = 1.36^{+0.3}_{-0.36}$ eV. The large hydrogen column and small size of the remnant favor the further distance of 11 kpc, which we adopt here. We note that MIPS 24 μm observations show diffuse emission covers the remnant, likely due to a foreground H II region to the northwest.

G348.5−0.0. An overlapping radio shell detected adjacent to CTB 37A, the SNR G348.5−0.0 appears to be a kinematically distinct interacting remnant. Both CO and OH maser observations indicate interaction with a cloud at −20 km s^{-1} for G348.5−0.0, whereas CTB 37A is found at −65 km s^{-1} (Frail et al. 1996; Reynoso & Mangum 2000). A line-of-sight magnetic field strength of −0.8 ± 0.1 mG is measured for a maser in G348.5−0.0 (Brogan et al. 2000). The near/far distance ambiguity for both G348.5−0.0 and CTB 37A is resolved in favor of the far distance by the H I observations, but not with sufficient resolution to differentiate between the two bright radio sources (Caswell et al. 1975). Archival *ASCA* observations did not allow a determination of the hydrogen column density toward G348.5−0.0, so using the established kinematic velocity of −22.0 km s^{-1} we integrated the total CO and H I column densities to estimate a column of 2.8 × 10^{22} cm^{-2} toward the remnant.

G349.7+0.2. The most luminous and distant SNR within the galaxy with detected OH(1720 MHz) masers is G349.7+0.2. Numerous molecular transitions indicative of shock interaction are detected toward including ^{13}CO, ^{12}CO, CS, H_2, HCO^+, HCN, H_2CO, and SO (Lazendic et al. 2004). A kinematic distance of G349.7+0.2 places it at 22 kpc, but rotation curves at such a large Galacto-centric radius are not well constrained. X-ray observations yield a neutral hydrogen column of 5.8 × 10^{22} cm^{-2} and suggest an age of only 3500 years (Lazendic et al. 2005). Frail et al. (1996) identified five maser spots at velocities

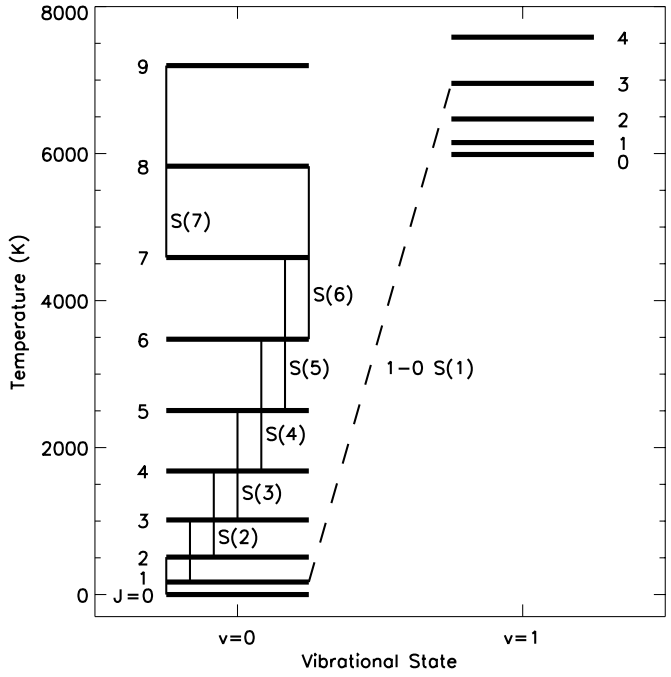

Figure 5. Rovibrational energy level diagram for molecular hydrogen with rotational J states labeled. The S(0)–S(7) transitions available to *Spitzer* low-resolution IRS observations are indicated with solid lines. All 'S' transitions are from the upper to lower J state with $\Delta J = 2$. The $v = 1$–0 S(1) transition commonly observed at 2.12 μm is plotted as a dashed line. Note that the S(7) transition traces a higher upper excitation state than the 1-0 S(0) and S(1) lines commonly observed in the NIR.

between +14.3 km s^{-1}and +16.9 km s^{-1}. The impacted cloud appears at $v_{\rm LSR} = +16.2$ km s^{-1} with a linear size of about 7 pc, a mass of 104 $M_\odot$, and a volume density of $\sim 10^3$ cm^{-3} (Dubner et al. 2004). The SNR–cloud interaction is thought to be taking place on the far side of the SNR from a comparison between total absorbing column density and slightly redshifted wings in the optically thin ^{13}CO spectra. Figure 4 shows the IRS LL2 spectra across the remnant. Bright H_2 S(1) and [Fe II] lines are seen associated with only the SNR shell. Though some [Ne III] and [S III] is present from diffuse interstellar emission outside the remnant, both lines are clearly enhanced coincident with the bright shell.

3.3. Excitation of Molecular Hydrogen

The bright emission from the H_2 S(0)–S(7) lines present in all six SNRs is an excellent diagnostic of the physical conditions of the shocked gas, of which H_2 is the dominant constituent. The energy level diagram for H_2 is presented in Figure 5 with the transitions observed by *Spitzer* labeled (by conventional branch notation S indicates $\Delta J = -2$). As these lines are optically thin, they provide a direct measure of the column density for each upper state $J_u = 2$ to 9. We note the S(7) transition has a rotational energy higher than that of the bright H_2 1–0 S(1) line typically observed in the NIR.

Rotational diagrams from de-reddened H_2 line intensities are presented in Figure 6. Here, the column density per magnetic substate is plotted against the upper energy level, such that a single temperature distribution in LTE follows a straight line. It is clear that a simple LTE excitation model for the observed level populations cannot fit both the positive curvature resulting from a range of gas temperatures, or the zig-zag pattern between subsequent ortho- and para-states out of equilibrium. However,

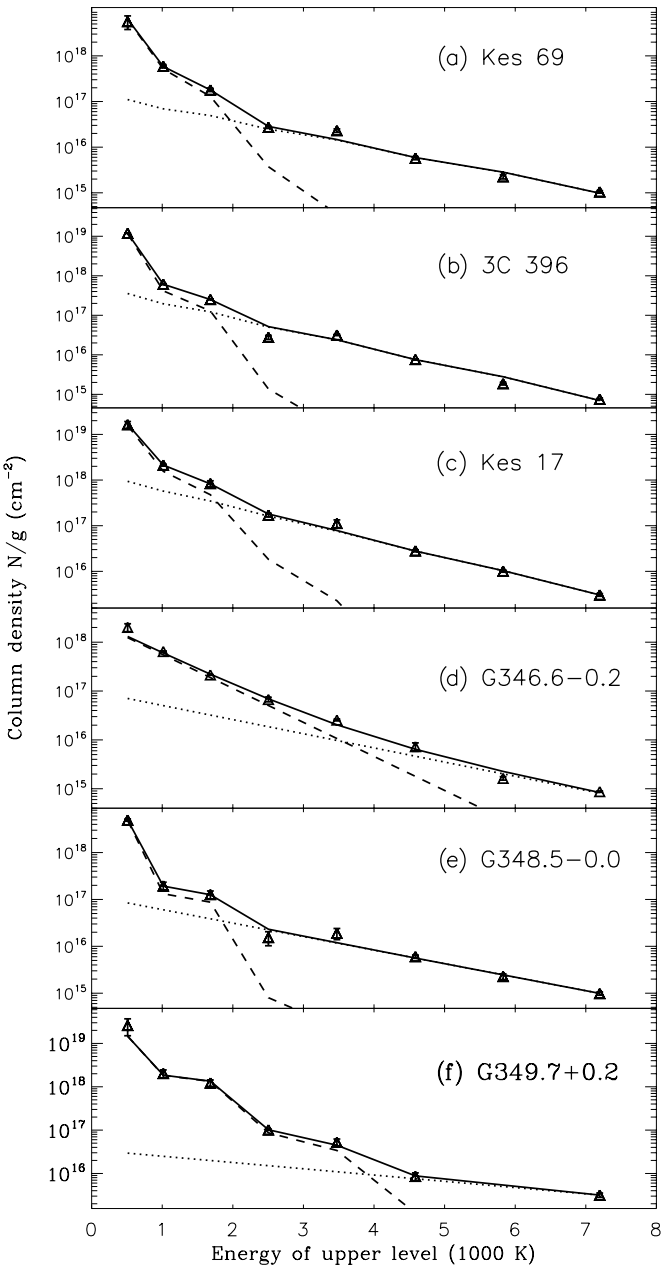

Figure 6. Boltzmann diagram for the excitation of H_2. From top to bottom: (a) Kes 69, (b) 3C 396, (c) Kes 17, (d) G346.6−0.2, (e) G348.5−0.0, and (f) G349.7+0.2. Triangles mark the column density of the upper J state obtained from the de-reddened brightness with error bars. The best-fit two-component model is overplotted as a solid dark line. A dashed line shows the contribution of the warm component, while a dotted line shows the contribution of the hotter component. Parameters for the fits are given in Table 5.

Table 5
Fitted Excitation Parameters to Observed Molecular Hydrogen Lines

Parameter	Kes 69	3C 396	Kes 17	G346.6−0.2	G348.5−0.0	G349.7+0.2
$N(H_2)_{\rm warm}$	1.5E20	3.0E20	3.8E20	4.7E19	1.2E20	2.8E20
$T_{\rm warm}$ (K)	303	265	322	528	261	467
$\rm OPR_{warm}$	1.3	0.65	1.4	3.0	0.4	0.99
$N(H_2)_{\rm hot}$	5.0E18	6.9E18	2.6E19	8.3E18	2.4E18	5.2E18
$T_{\rm hot}$ (K)	1465	1270	1152	1241	1773	1647
$\rm OPR_{hot}$	3.0	3.0	2.5	3.0	3.0	3.0

it is instructive to examine the properties of a two-temperature model which can be well fit to the data. Table 5 gives the

best fits from least squares fitting assuming two temperature distributions and simple LTE excitation of H_2. Common for the fits are a warm component with $T_w \sim 250$–600 K and a column $N_w \sim 10^{20}$ cm^{-2}, and a hot component with $T_h \sim 1000$–2000 K and a column $N_w \sim 10^{19}$ cm^{-2}. In Figure 6, the warm component is drawn as a dashed line, the hotter component is drawn as a dotted line, and the total contribution as a solid line. For the hotter gas component (the dotted line), the ortho-to-para ratio (OPR) is found to be at or near the statistical equilibrium value of 3. However, the warm component (the dashed line) shows OPR between 0.4 and 3, manifested as zig-zags between ortho- and para- levels in the energy diagrams. This large range in OPR_w was also found for the interacting SNRs 3C391, IC 443, W28, and W44 (Neufeld et al. 2007). The conversion of ortho to para in shocks is strongly dependent on temperature, with threshold temperatures at 700 K to start conversion and 1300 K to rapidly reach the equilibrium value (Timmermann 1998). The temperature of warm gas is substantially less than 700 K for all but SNR G346.6−0.2 which has an OPR_w of 3. For the other remnants, an OPR between 0.4 and 1.4 is characteristic of an equilibrium temperature between 50 and 100 K. For shock velocities $\lesssim 20$ km s^{-1}, the H_2 gas will retain the OPR of the preshock gas, with only a small dependence on gas density (Wilgenbus et al. 2000). Low OPR values indicate that there has not been substantial preheating of the preshock material with which these SNRs are now interacting.

4. SHOCK MODELS

At the position of the bright IR peak observed in each SNR, both strong molecular and ionized species are present. This discordant mix of spectral lines cannot be reconciled with a single shock into a uniform medium. We consider two general classes of shock models. Jump (J) shocks have a discontinuous change of hydrodynamic variables, with heating over a negligible thickness sufficient to dissociate molecules (Hollenbach & McKee 1989). It is possible for H_2 and other molecules to reform in the cooling postshock region. In contrast continuous (C) shocks have a transition region in which friction between ions and neutrals occurs over a sufficiently large thickness that the transition from pre- to postshock is continuous and nondissociative for molecular gas of modest ionization (Draine et al. 1983). In the following sections, we consider the physical parameters of shocks which can explain the observed IR line emission.

4.1. H_2 Rotational Lines

For each remnant, the observed H_2 columns are compared to published C- and J-shock models. The H_2 line intensities, particularly at low excitation temperatures, are typically more than an order of magnitude brighter than predicted by J-shock models (e.g., Hollenbach & McKee 1989). A comparison with C-shock models (e.g., Draine et al. 1983) shows lines of comparable magnitude, but a single C-shock could not simultaneously account for the strengths of all observed H_2 lines.

Using a grid of shock models, a detailed fit to the excitation of H_2 lines was performed using least squares fitting. The relevant shock variables are shock velocity v_s and preshock density n_o. Two recent C-shock models were used. The first model of Wilgenbus et al. (2000) accounts for the nonequilibrium OPR observed in the warm H_2 gas. A grid of computed models spans $(\log_{10} n_o) = 3, 4, 5, 6$ cm^{-3}, $v_s = 10, 15, 20, 25, 30, 40$ km s^{-1}, and OPR $= 0.01, 1, 2, 3$. For shock velocities above a certain critical velocity H_2 is dissociated; without H_2, cooling a continuous transition cannot be sustained and the shock becomes J-type. Le Bourlot et al. (2002) found that C-shocks could be sustained at much higher velocities than previously thought, ranging up to 23–80 km s^{-1} for densities of 10^7 to 10^3 cm^{-3}, with increments matching those of Wilgenbus et al. (2000). The second shock model from Le Bourlot et al. (2002) correctly accounts for shock speeds up to the critical velocity but assumes OPR = 3. However, for shock velocities much less than the critical velocity ($\sim$ 10–20 km s^{-1}) there is good agreement between the work of Le Bourlot et al. (2002) and Wilgenbus et al. (2000) for OPR = 3. Together these two sets of models form a grid of C-shock models that span the observed H_2 excitation parameters found in Section 3.3.

In our model fitting, each shock component is given a free-linear scaling to account for uncertainty in the geometry and area of the shock relative to the IRS aperture. This factor Φ_s is the ratio of the projected beam size to the surface area of the shock. If the beam is not completely covered by shocked material, the value of Φ_s can be less than unity.

No single shock model is found that can reproduce the positive curvature observed in the Boltzmann diagrams. For a good fit to the data, a combination of two shock models is required. A slow C-shock gives a good fit to the lower excitation lines (e.g., H_2 S(1)) but underpredicted the observed brightness of higher excitation lines (e.g., H_2 S(7)). In addition to C-shocks, we included the J-shock models of Hollenbach & McKee (1989) as a discontinuous grid of models with densities of 10^3–10^6 cm^{-3} and shock velocities of 30–150 km s^{-1} in 10 km s^{-1} increments. The results using a single C-shock with either a second faster C-shock or a fast J-shock are given in Tables 6 and 7. Figure 7 shows the best fits to the observed excitation of each SNR which are generally found to be two C-shocks.

We find a slow $\sim$ 10 km s^{-1}, dense $\sim 10^6$ cm^{-3} C-shock gives an excellent fit to the S(0)–S(3) lines, including non-LTE OPR. The higher excitation lines are well fit by a fast C- or J-shock through a lower-density medium ($n_o \sim 10^4$ cm^{-3}, $v_s \sim$ 30–60 km s^{-1}), in which the OPR is quickly brought to equilibrium. In general, a fast C-shock gives a better fit to the observed excitation of H_2 than a fast J-shock. The only exception is G346.6−0.2, in which a single C-shock at a velocity of $\sim$ 15km s^{-1}into a density of 10^{5-6} cm^{-3} and an OPR of 3 reproduces the observed H_2 S(0)–S(6) lines but underestimates the H_2 S(7) line. Either a fast C-shock or a fast J-shock into a lower density medium can produce the S(7) line, but this shock component is not well constrained, so either solution is viable. Figure 8 shows the alternative J-shock solution given in Table 8. For all other remnants, a C- and J-shock combination does not do a good job or reproducing the observed excitation; however, we do list the best-fit parameters in Table 7 for comparison with the two C-shock models. It is possible that our best fit of two C-shock models is a characteristic of temporal evolution of an MHD shock (Chieze et al. 1998; Cesarsky et al. 1999).

To check the validity of fitting results and to understand associated physical processes, we compare the shock model fits to a simple analytic treatment of energy conservation in C-shocks (Neufeld et al. 2006, Appendix B). The characteristic gas temperature of a C-type shock is given by

$$T_s = 375\, b^{-0.36} (v_s/10 \text{ km s}^{-1})^{1.35} \text{ K}, \quad (1)$$

where $b = \text{B}/\mu\text{G}\, (n_o/\text{cm}^{-3})^{-0.5}$. Given the standard assumption that $b = 1$, the warm and hot gas components discussed in Section 3.3 typically correspond to shock velocities of $\sim$ 10 and

Table 6
Combination of Two C-Shock Model Fits

Parameter	Kes 69	3C 396	Kes 17	G346.6−0.2	G348.5−0.0	G349.7+0.2
C-shock 1						
n_0 (cm^{-3})	10^5	10^6	10^6	10^6	10^5	10^6
v_s (km s^{-1})	10	10	10	15	10	10
Φ_s	0.043(4)	0.089(2)	0.28(3)	0.055(2)	0.095(9)	0.61(3)
OPR	1	2	1	3	1	1
P_s (dyn cm^{-2})	2×10^{-7}	2×10^{-6}	2×10^{-6}	4×10^{-6}	2×10^{-7}	2×10^{-6}
$N(H_2)$ (cm^{-2})	4.3E20	5.4E19	2.0E20	2.1E19	1.0E20	4.1E20
C-shock 2						
n_0 (cm^{-3})	10^4	10^5	10^4	10^5	10^4	10^5
v_s (km s^{-1})	40	30	40	50	40	40
Φ_s	0.029(1)	0.0091(1)	0.094(1)	0.004(1)	0.024(1)	0.0071(7)
P_s (dyn cm^{-2})	3×10^{-7}	1.5×10^{-6}	3×10^{-7}	4×10^{-6}	3×10^{-7}	3×10^{-6}
$N(H_2)$ (cm^{-2})	1.5E20	2.6E18	5.0E20	3.5E24	1.3E20	7.1E19

Notes. Errors to fitted shock models are found to be approximately 0.5 for gas density $\log_{10} n$, 5 km s^{-1} for shock velocity v_s, and less than 10% for Φ_s.

Table 7
Combination of C- and J-Shock Model Fits

Parameter	Kes 69	3C 396	Kes 17	G346.6−0.2	G348.5−0.0	G349.7+0.2
Slow C-shock						
n_0 (cm^{-3})	10^6	10^6	10^6	10^6	10^6	10^6
v_s (km s^{-1})	10	15	10	15	15	10
Φ_s	0.132	0.046	0.13	0.053	0.064	0.54
OPR	2	2	2	3	1	1
P_s (dyn cm^{-2})	2×10^{-6}	4×10^{-6}	2×10^{-6}	4×10^{-6}	4×10^{-6}	2×10^{-6}
Fast J-shock						
n_0 (cm^{-3})	10^3	10^4	10^3	10^4	10^3	10^4
v_s (km s^{-1})	90	130	50	150	60	110
Φ_s	0.104	0.005	0.19	0.0053	0.057	0.10
P_s (dyn cm^{-2})	1.4×10^{-7}	3×10^{-6}	4×10^{-8}	3×10^{-6}	6×10^{-8}	2×10^{-7}

Table 8
Comparison of Model Fitting for Single and Multiple Shocks

Model SNR	One C-shock (n_0, v_s) [χ_r^2]	Two C-shocks (n_0, v_s),(n_0, v_s) [χ_r^2]	Two $n_0 = 10^4$ C-shocks (n_0, v_s),(n_0, v_s) [χ_r^2]	C- and J-shock (n_0, v_s),(n_0, v_s) [χ_r^2]
Kes 69	(10^5,20)[60]	**(10^5,10),(10^4,40)[12]**	(10^4,20),(10^4,50)[24]	(10^6,10),(10^3,90)[20]
3C 396	(10^6,15)[56]	**(10^6,10),(10^5,30)[8.0]**	(10^4,20),(10^4,40)[23]	(10^6,15),(10^4,130)[65]
Kes 17	(10^5,30)[23]	**(10^6,10),(10^4,40)[4.1]**	(10^4,20),(10^4,40)[5.4]	(10^6,10),(10^3,50)[48]
G346.6−0.2	(10^6,15)[14]	(10^6,15),(10^5,50)[7.0]	(10^4,30),(10^4,50)[4.9]	**(10^6,15),(10^4,150)[0.9]**
G348.5−0.0	(10^6,20)[15]	**(10^5,10),(10^4,40)[2.4]**	(10^4,10),(10^4,40)[4.4]	(10^6,10),(10^3,60)[12.4]
G349.7+0.2	(10^6,15)[16]	**(10^6,10),(10^4,50)[0.6]**	(10^4,20),(10^4,50)[6.3]	(10^6,10),(10^4,110)[2.9]

Notes. [a] Values in the brackets are reduced χ_r^2. The best solution is in bold.

$\sim$ 30 km s^{-1}, respectively. This is in general agreement with the parameters fit in the modeling, however the hot gas shock velocity is typically found to be somewhat higher. The observed column density of shocked H_2 is given by

$$N_s = 4 \times 10^{20}\, b\, n_{04}^{0.5}\, (v_s/10\ \mathrm{km\ s})^{-0.75}\, \Phi_s, \qquad (2)$$

where the preshock density is $10^4 n_{04}$ cm^{-3}, and Φ_s is the ratio of the projected beam size to the surface area of the shock as before. Even though the preshock density n_o is not well constrained by the low-J rotational transitions, a comparison between the H_2 column for the warm and hot component in Table 5 and the expected value of N_s/Φ_s from Equation (2) can establish whether the fitted Φ_s is reasonable. Using the best-fit model preshock density and shock velocity in Table 6, we find the expected values of Φ_s match the model-fitted Φ_s within a factor of a few. Typically, Φ_s is found to be 0.1–0.5 and 0.03–0.02 for the warm-slow and hot-fast shocks, respectively. For Herbig–Haro objects, there is significant substructure not resolved by IRS, and values of Φ_s for the warm and hot components are typically $0.2 n_{04}^{0.5}$ and $0.05 n_{04}^{0.5}$ (Noriega-Crespo et al. 2002; Neufeld et al. 2006). Supernova remnants also appear to have significant substructure which IRS observations are not able to resolve.

We now compare the shock models of that fit of our H_2 lines with other models and observations. Le Bourlot et al (2002) applied C-shock models to the H_2 lines from Orion, and found a best fit with $n_o = 10^4$ cm^{-3} and two different shock velocities of 40 and 60 km s^{-2}. Table 8 shows that two different density models yield a better fits than two different velocities for a single density. Burton (1992) suggested a density of 10^6 cm^{-3} with a very low velocity of 10 km s^{-1}; such a model cannot explain all the higher-J observed H_2 emission (see the dashed and dotted lines in Figure 7). Richter et al. (1995) suggest partially

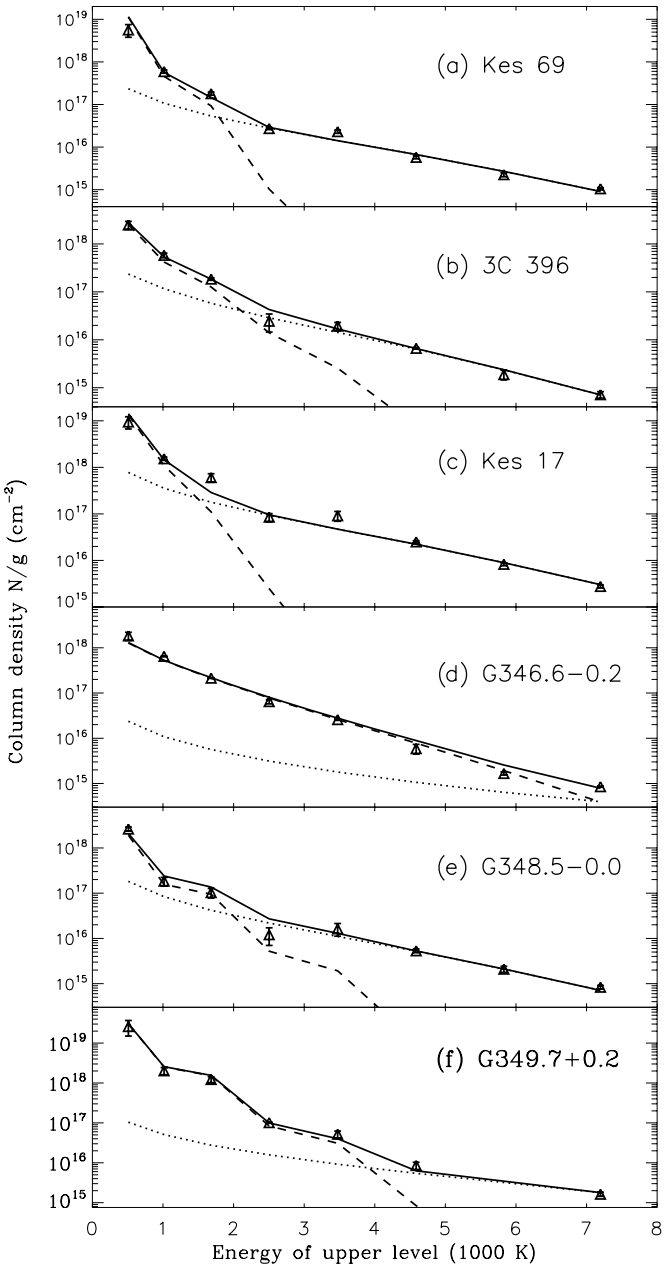

Figure 7. Two C-shocks are fitted to the observed excitation of H_2. From top to bottom: (a) Kes 69, (b) 3C 396, (c) Kes 17, (d) G346.6−0.2, (e) G348.5−0.0, and (f) G349.7+0.2. The total of two fitted shock components is overplotted as a solid line. A dashed/dotted line shows the contribution of the slower/faster shock. Parameters for the fits are given in Table 6.

dissociated H_2, from a J-shock, but the implied high velocities could not be explained. Fits to ISOCAM observations of IC 443 show a density of 10^4 cm^{-3} with excitation temperatures of 330–657 K and 1115–1300 K (Cesarsky et al. 1999). Our fit results show two main differences from those of Cesarsky et al. (1999); one is a higher density component and the other is departure from LTE OPRs. The main differences may arise from our inclusion of S(0) and S(1) lines which could not be observed by ISO. The departure from LTE is independent of shock models and implied by the two temperature fitting of H_2 excitation diagram. The inferred OPRs are out of equilibrium indicating the timescale of the shock passage was too short to establish equilibrium (Pineau Des Forêts & Flower 2000). In the course of shock passage, temporal nonequilibrium could be because of dynamical processes with colder gas, or fast conversion of ortho-H_2 to para-H_2 during the formation on the surface of grains. Molecular hydrogen formation is mainly governed by the properties of grain surfaces and shocked medium quickly accreted in the diffuse ISM in even a modest velocity ($\sim$ 30 km s^{-1}) shock (Jones et al. 1994; Cazaux & Tielens 2002). A combination of two C-shock models indicates a shock into very dense (10^{5-6} cm^{-3}) gas with a low (10–15 km s^{-1}) shock velocity where sputtering and dust destruction may not be as efficient.

Given a multiphase ISM, a combination of preshock densities is possible. At moderate density (10^3–10^4 cm^{-3}), faster shock component has been resolved in W44 and W28 (Reach & Rho 2000). Widths of H_2 in the shock front are measured to be $\sim 10^{16}$ cm, consistent with nondissociative shocks into gas with densities of $\sim 10^4$ cm^{-3}. These densities are consistent with our fast C-shock component of 40–70 km s^{-1} (see Table 6). Perhaps surprisingly, the slower, denser shock has a larger filling factor than this faster, lower density shock in our fitting. At such high densities of 10^5–10^6 cm^{-3}, cooling will be faster with a lower peak temperature and a larger shock thickness if the two shocks are roughly isobaric. Cooling could be significant from molecular lines other than H_2 (such as H_2O), though the current observations are not sufficient to detect such lines, for which observations with a higher resolution spectroscopy are required.

4.2. Ionic Lines

Strong ionic lines are observed toward all SNRs and cannot be reproduced by steady state C-shock models (see Draine et al. 1983). We use the J-shock models to derive the shock velocity and preshock density purely from consideration of the surface brightness of observed ionic lines. Here, our purpose is to determine the gross properties of the fast J-shock responsible for the observed fine-structure lines[3].

Diagnostics of the [Fe II] lines use excitation rate equations, which are presented in Rho et al. (2001). Figure 9 shows contours of line ratios of 17.9/5.35 μm and 17.9/26 μm; the former ratio is sensitive mainly to density and the latter ratio changes depending on both density and temperature. Updated atomic data (Ramsbottom et al. 2007) affected (at the <10% level) the contours at low densities (<200 cm^{-3}). The estimated density and temperatures from [Fe II] ratios are summarized in Table 9. A set of electron density and temperature solutions is possible for each of G349.7+0.2 and 3C 396: (n_e, T) = (700 cm^{-3}, 7000 K) and (270, 2.3 $\times$ 10^4), respectively. The ratio of Kes 17 indicates (n_e, T) = (100, 7000) showing a low electron density. For Kes 69 and G348.5−0.0, the two ratios did not converge; the ratio of [Fe II] 17.9/5.35 μm indicates a higher temperature than that from the ratio of [Fe II] 17.9/26 μm. This may be because of either uncertainties of collisional strengths at low density and temperature or presence of multi-temperature gas. The ratio of [Fe II] 17.9/5.35 μm indicates a low density (<400 cm^{-3}) and low temperature (<2000 K). Temperature could not be well constrained; lines of higher upper energy

[3] The [Fe II] 26 μm is prominently detected, but the spectral resolution of IRS is not sufficient to distinguish between the [O IV] 25.9 and [Fe II] 26 μm lines. Observations of interacting remnants with ISO and IRS at high spectral resolution are able to separate the two lines, and find that the [O IV] 25.9 μm line does not contribute significantly if at all to [Fe II] 26 μm line flux (Reach & Rho 1999; Neufeld et al. 2007). Furthermore, the [O IV] 25.89 μm line has an ionization potential of 54.9 eV and is significant only for very fast shocks in excess of those observed here. We expect that the [Fe II] 25.98 μm line is by far dominant for most, if not all, of the SNRs we consider here.

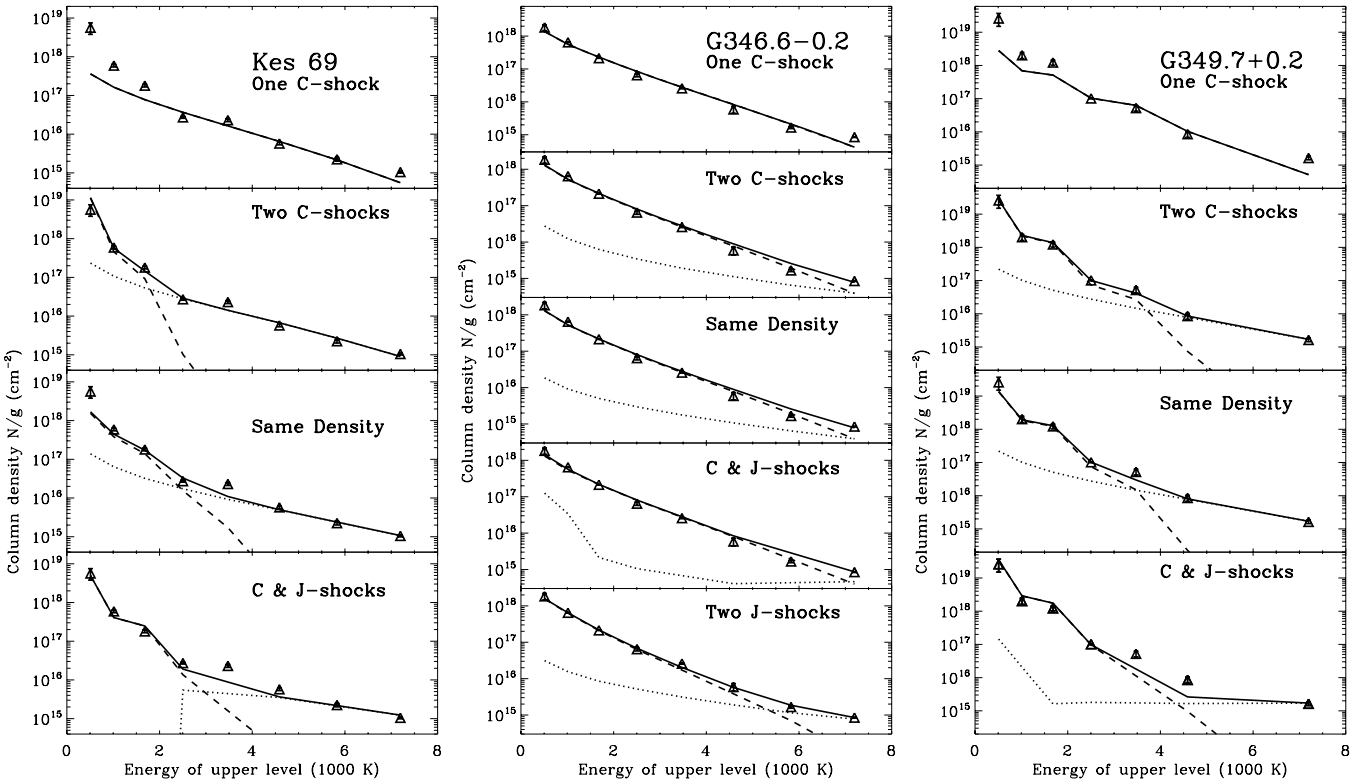

Figure 8. Comparison of fitted shock models to excitation of H_2 by a combination of shocks for Kes 69 (left), G346.6−0.2 (center), and G349.7+0.2 (right). From top to bottom: a single C-shock, two C-shocks with different densities and velocities, two C-shocks with the same density of 10^4 cm^{-3}, a combination of one C-shock and one J-shock. Table 8 has the fitted values and reduced chi-squared values. In cases of multiple shocks, the slower shock is plotted with a dashed line and the faster shock with a dotted line. The total contribution of the two shock components is plotted as a solid line.

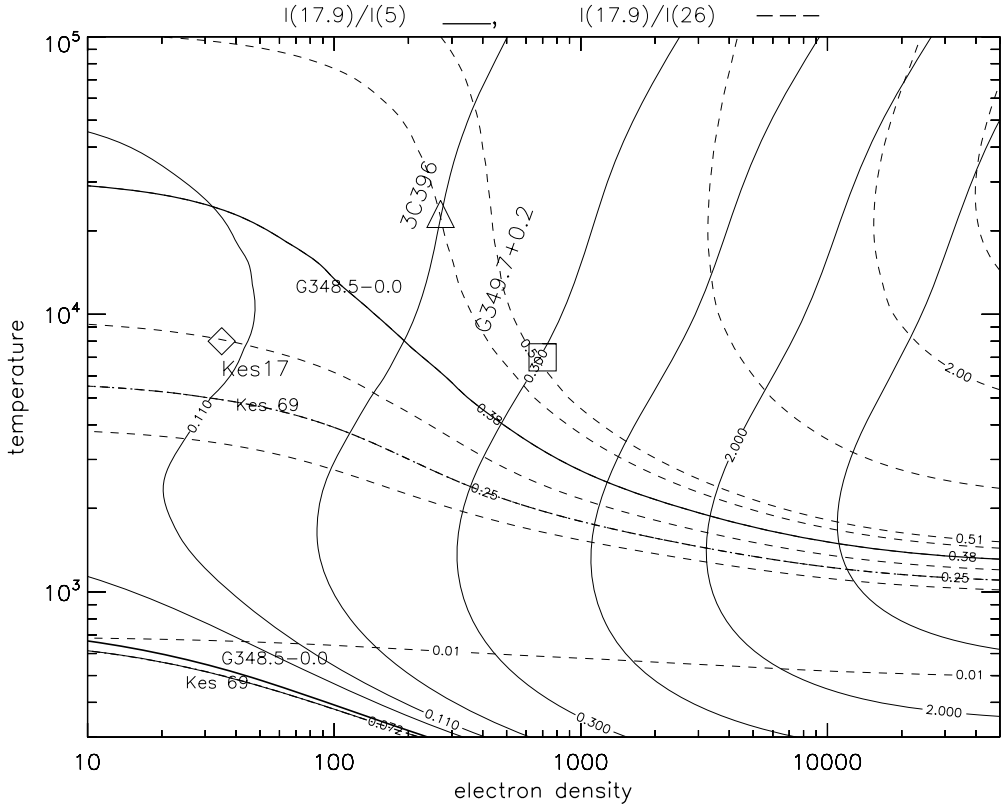

Figure 9. Contour plots of [Fe II] diagnostic line ratios using 5.3, 17.9, and 26 μm lines. The observed ratios of G349.7+0.2 (square), 3C 396 (triangle), and Kes 17 (diamond) are marked. The two ratios for Kes 69 (two thick dotted lines) and G348.5−0.0 (two thick solid lines) do not converge to the same temperature and density ranges which may be because of uncertainties of collisional strengths at low density and temperature or presence of multitemperature components.

Table 9
Physical Properties Derived from Ionic Line Diagnostics

(source)[a]	[Fe II] Ratios		[Si II], [Fe II], [Ne II] lines		[Ne III]/[Ne II]	V_s	Pressure[b]
SNR Name	n_e (cm^{-3})	T(K)	n_o (cm^{-3})	v_s (km s^{-1})	v_s (km s^{-1})		(dyn cm^{-2})
Kes 69	multi-T or n_e[c]		500–1000	150	150	150	2.8×10^{-7}
3C 396	270	23000	500–1000	100–150	350	120, 350	1.8×10^{-7}, 1.5×10^{-6}
Kes 17	100	7000	500–1000	150	150 or 200	150	2.8×10^{-7}
G346.6−0.2	...	...	100–200	70–100	80	80	1.1×10^{-8}
G348.5−0.0	multi-T or n_e[c]		500–1000	160	160	160	3.2×10^{-7}
G349.7+0.2	700	7000	10^4	250	80 or 250	250	1.0×10^{-5}

Notes.
[a] Denotes which ionic lines were used to derive the density, temperature, or shock velocity.
[b] The pressure is estimated based on n_o and V_s derived from Si, Fe, and Ne lines and from [Ne III]/[Ne II] ratio.
[c] Possible multi-temperature and multi-density solution (see Figure 8); the ratio of [Fe II] 17.9/5 μm yields a low density (<400 cm^{-3}) and low (<2000 K) temperature.

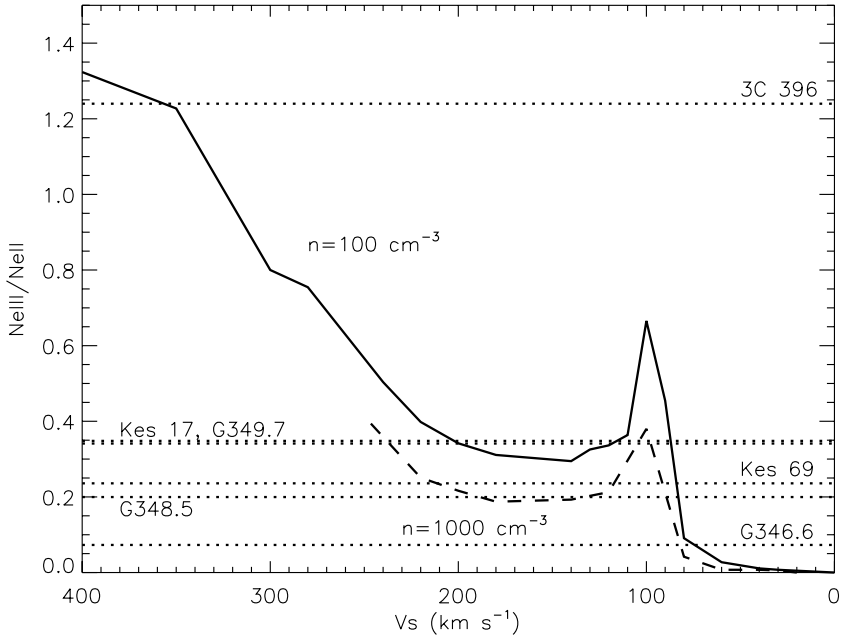

Figure 10. Predictions from the models of Hartigan et al. (1987) of the [Ne III] 15.5/[Ne II] 12.8 μm ratio as a function of shock velocity for densities of 100 and 1000 cm^{-3}. The observed values for each remnant are marked as dashed lines.

levels such as the [Fe II] 1.64 μm line are required to constrain temperature.

The preshock medium density n_o and shock velocity v_s are also constrained using the strength of the [Ne II] 12.8, [Si II] 34.8, [Fe II] 26 μm lines (called the three main ionic lines hereafter, see Figure 6 of Rho et al. 2001 which was generated based on Hartigan et al. 1987 and McKee et al. 1984). The inferred medium densities and shock velocities are summarized in Table 9. Iron lines have a high ionization potential, and may not arise from the same physical conditions as these ionic lines with lower ionization potentials.

The ratio of [Ne III] 15.5/[Ne II] 12.8 is also useful in determining shock velocity and is presented in Figure 10 with results summarized in Table 9. The inferred shock velocities from Ne ratios are generally consistent with those from the brightnesses of three main lines except 3C 396. The only remnant for which the Ne III/Ne II ratio is greater than unity is 3C 396, suggesting a shock in excess of 300 km s^{-1}, while the inferred shock velocity from the line intensities of [Si II], [Fe II], [Ne II] is 100–150 km s^{-1}. The [Ne III] in 3C 396 may arise from fast shocks than the lower-ionization state lines.

4.3. Molecular and Ionic Shocks and Ejecta Contribution

Estimates of the shock ram pressure (P_s) can be derived from the shock modeling in the previous two sections. The best-fit parameters from both C-shocks derived from H_2 and the fast and diffuse J-shock traced by ionic lines are given in Tables 6 and 9, respectively. The highest pressures are generally experienced in the molecular C-shocks in which the postshock gas cools and condenses and can obtain a pressure higher than the thermal pressure of the remnant proportional to the gas compression factor (Moorhouse et al. 1991). It is well established theoretically that pressure enhancements of 10–100 times can occur when the SNR shell interacts with dense clumps (Chevalier 1999). The OH maser emission was detected from Kes 69, G348.5−0.0, G346.6−0.2, and G349.7+0.2, which is evidence of the survival of higher density clumps. We caution that the pressures derived from shock models may have uncertainties up to an order of magnitude. Given this large uncertainty, it is still clear that H_2 emission originates from regions where the pressure is of order 10^{-7}–10^{-6} dyn cm^{-2}. The pressures derived for each of the two C-shock components

is consistent with an isobaric shock into a multiphase cloud with a range of densities. In general, the pressure derived from the three ionic lines is comparable to that derived for the C-shocks, though the densities are lower (100–1000 cm^{-3}) and shock velocities higher. Again this is consistent with the SNR shock interacting with a multiphase MC with both an ambient molecular phase and a dense clump phase (Reach & Rho 2000).

There are a few exceptions to the general observations above. G349.7+0.2 has an exceptionally high ionic shock ram pressure, even exceeding that of the dense C-shocks. The bright ionic lines, inferred high shock velocity and a high electron density inferred from [Fe II] line suggest that this SNR is younger than other SNRs in our sample, and may contain a contribution from SN ejecta. X-ray observations also show abundance enhancements indicative of a significant ejecta mass (Lazendic et al. 2005), and the estimated age of the SNR is 3500 yr.

Another exception is G346.6−0.2, where only very weak ionic lines and OPR of 3 are observed. The ionic pressure is estimated to be only $\sim 10^{-8}$ dyn cm^{-2}, whereas the pressure from the C-shocks is both 4×10^{-6} dyn cm^{-2}. Given that the OPR is observed at equilibrium, this may suggest that the shock has had sufficient time to establish a steady state C-shock, whereas those remnants with nonequilibrium OPR and observed ionic emission may have not yet obtained steady state. The weak ionic lines appear to arise from a shock into a low density ambient medium of 100 cm^{-3} and not the dense clump material from which H_2 emission originates.

Finally, 3C 396 shows a large range of pressures. The pressure of the hot thermal X-ray gas observed in the interior of the SNR is estimated to be of order 3×10^{-9} dyn cm^{-2} (Harrus & Slane 1999). This is a factor of a few smaller than the shock pressure derived from ionic line diagnostics 1.8×10^{-7} dyn cm^{-2}. In comparison to the observed H_2 emission from 3C 396, the shock pressure is observed to be a factor of $\sim$ 10 higher. Given the spatial segregation of the ionic and H_2 lines, it is plausible that H_2 emission is arising from interaction with dense clumps, while emission from the main ionic lines arises from the same shock propagating into a lower ambient density medium or contribution from ejecta. The fact that Fe line emitting gas is possibly hotter and denser than the other four SNRs (see Table 9) and the two different shock velocities supports the view that the infrared emission from 3C 396 is composed of both ejecta fragments and shocked ISM. A full spectral mapping (such as of Cas A; Rho et al. 2008) would be required to separate distribution of ejecta and shocked ISM.

5. DIFFUSE WARM H_2

Warm diffuse H_2 gas is known to be abundant throughout the galaxy (Gry et al. 2002; Falgarone et al. 2005). Diffuse H_2 emission has also been noted at the SNR–cloud interaction site, though its relation to the shock interaction is unclear (Neufeld et al. 2007). Using careful local background subtraction, we are able to isolate the H_2 emission only due to the supernova remnant interaction. We find enhanced S(0) and S(1) emission from the shock interaction, but often the diffuse emission is dominant. Here, we discuss the excitation of this warm diffuse molecular gas.

Diffuse S(0) and S(1) lines are detected for nearly every sight line, including our sky reference positions. The diffuse component we observe could arise from conditions in the preshock clouds or from low density diffuse gas present along the line of sight through the Galaxy. Several excitation mechanisms for warm diffuse H_2 present in the Galactic plane have been proposed including the Galactic radiation field, H_2 formation energy (Spitzer 1974), and MHD shocks or small-scale turbulence (Falgarone et al. 2005). However, higher energy transitions such as S(2)–S(7) are not detected as for the SNRs. Because we have only one ortho and one para line, the ortho-to-para ratio and gas temperature are degenerate, so we can only constrain the excitation of diffuse H_2.

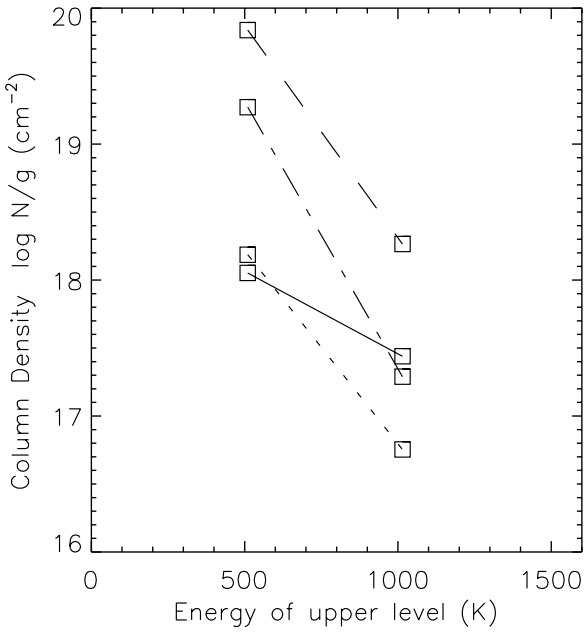

Figure 11. Boltzmann diagram for the excitation of diffuse H_2 observed toward four SNRs in our sample. Each SNR is plotted with a different line-style: dotted for 3C 396, solid for G346.6−0.2, dash-dotted for G348.5−0.0, and dashed for G349.7+0.2.

Table 10
Fitted Physical Conditions of Diffuse H_2

Parameter	3C 396	G346.6−0.2	G348.5−0.0	G349.7+0.2
N_{H_2}(cm^{-2})	2.1e20	5.3e19	4.3e21	6.4e21
T(K)	155	361	118	154
OPR	≡ 3.0	≡ 3.0	≡ 3.0	≡ 3.0
N_{H_2}(cm^{-2})	1.2e20	3.6e19	2.40e21	3.6e21
T(K)	177	509	130	176
OPR	≡ 2.0	≡ 2.0	≡ 2.0	≡ 2.0
N_{H_2}(cm^{-2})	3.3e19		3.7e21	1.5e21
T(K)	292		222	233
OPR	0.65		0.4	0.99

Table 10 gives the fitted parameters to the warm diffuse H_2 emission in the regions used as a local background in data reductions. We have not included Kes 69 or Kes 17 as the slit of one of the LL orders lies almost entirely inside the SNR. As the temperature is degenerate with the ortho-to-para ratio, we have assumed a range of different OPR. In the first block of physical parameters listed in Table 10, we assume an OPR of 3.0 to derive excitation temperatures that range from 100 to 160 K, with the notable exception of G346.6−0.2. Figure 11 shows the Boltzmann diagram for diffuse emission from outside the SNRs. The slope of the line connecting the S(0) and S(1) transitions is markedly different for G346.6−0.2 than for the other remnants. Diffuse emission toward G346.6−0.2 may be associated with a foreground H II region which appears to dominate the MIPS 24 μm image of the SNR's vicinity.

The assumption of an ortho-to-para ratio of three gives the minimum temperature of the gas (see Table 10, row 1). At such

low temperatures the equilibrium OPR is roughly two and may be a more appropriate value. However, if the diffuse warm H_2 has only been recently heated from a colder, quiescent state, it could have a significantly lower OPR. For comparison with the shocked gas, we use the OPR of the warm shocked gas listed in Table 5. These solutions for various ortho-to-para ratios are all given in the second block of parameters listed in Table 10.

Even for the lowest OPR (the third block of parameters listed in Table 10), which is taken to be the same as that observed for the SNR shock, the excitation temperature of the low-lying rotation transitions is comparable to the 180–390 K excitation temperatures observed by Savage et al. (1977) in a study of UV absorption sight lines. Falgarone et al. (2005) report on the excitation of S(0)–S(3) transitions for a line of sight devoid of massive star-forming regions, finding comparable surface brightness for the S(1) and S(0) transitions. As we did not detect the S(2)–S(7) lines for the diffuse molecular gas, we were not able to probe these proposed signatures of dissipative turbulence.

Though the excitation conditions are somewhat uncertain, we are able to estimate the fraction of warm molecular gas to the total amount of molecular gas. Using the CO survey of Dame et al. (2001), we integrate the amount of CO along the line of sight toward the SNR. We estimate the total column of molecular hydrogen using the canonical conversion $N(H_2)/I_{CO} = 2 \times 10^{20}$ cm^{-2} (K km s^{-1})$^{-1}$. Though our apertures differ greatly, if the diffuse component is fairly uniformly distributed we can estimate a warm gas fraction. We find warm gas fractions of at least 0.005, 0.005, 0.15, and 0.08 toward SNRs 3C 396, G346.6−0.2, G348.5−0.0, and G349.7+0.2, respectively.

6. CONCLUSIONS

The nature of six SNRs identified as having molecular colors in the GLIMPSE survey have been resolved spectrally by *Spitzer* IRS observations. Strong H_2 S(0)–S(7) lines show clear evidence of shock interaction with dense gas. This doubles the number of known molecular remnants for which H_2 emission has been characterized. The excitation of H_2 is well fit by warm $T \sim 400$ K and hot $T \sim 1500$ K gas components. The OPR of the warm component deviates from equilibrium consistent with the passage of a slow shock through dense gas.

Ionic fine structure lines are also present for all SNRs but have large variations in brightness between the remnants. The presence of both strong molecular emission and ionic fine structure lines with large ionization potentials requires multiple shocks present within the observed aperture. In 3C 396, we see that the H_2 and ionic lines are spatially separated, indicating changing physical conditions across the shock front which agrees with a multiphase preshock medium composed of atomic, molecular, and dense clump gas.

A comparison of shock models shows that two C-shocks are required to explain the observed H_2 emission. Fitted shock parameters show one shock is of low velocity (~ 10 km s^{-1}) into dense gas ($\sim 10^6$ cm^{-3}), while another shock of higher velocity (~ 50 km s^{-1}) is propagating into lower density gas ($\sim 10^4$ cm^{-3}). Ionic lines require a fast J-shock into diffuse gas, typically with a density $\sim 10^3$ cm^{-3}. We find that physical conditions for these fast ionic shocks imply pressures similar to those found in the molecular C-shocks into dense clumps. For G349.7+0.2, we find extremely high ionic line pressures which are several times higher than for the H_2 emitting gas, possibly indicative of powerful ejecta shocks.

Long slit spectroscopy of these SNRs isolates diffuse emission from that of the remnant. This is particularly important for the H_2 S(0) and S(1) lines as well as diffuse interstellar cooling lines such as [Si II] 34.8 μm. We find the diffuse H_2 gas is relatively cool with a temperature of 100–300 K and a warm gas fraction of 0.5%–15%.

We thank Achim Tappe for updating atomic data and fruitful discussion on atomic Fe lines. This work is based on observations made with the *Spitzer Space Telescope*, which is operated by the Jet Propulsion Laboratory under NASA contract. J. W. Hewitt is grateful for the support of the IPAC staff and the Spitzer Visiting Graduate Student Program.

REFERENCES

Appleton, P. N., et al. 2006, ApJ, 639, L51
Brogan, C. L., Frail, D. A., Goss, W. M., & Troland, T. H. 2000, ApJ, 537, 875
Burton, M. G. 1992, Aust J Phys, 45, 463
Caswell, J. L., Murray, J. D., Roger, R. S., Cole, D. J., & Cooke, D. J. 1975, A&A, 45, 239
Cazaux, S., & Tielens, A. G. G. M. 2002, ApJ, 575, L29
Cesarsky, D., Cox, P., Pineau des Forêts, G., van Dishoeck, E. F., Boulanger, F., & Wright, C. M. 1999, A&A, 348, 945
Chevalier, R. A. 1999, ApJ, 511, 798
Chieze, J.-P., Pineau des Forets, G., & Flower, D. R. 1998, MNRAS, 295, 672
Dame, T. M., Hartmann, D., & Thaddeus, P. 2001, ApJ, 547, 792
Dickey, J. M., & Lockman, F. J. 1990, ARA&A, 28, 215
Draine, B. T. 2003, ARA&A, 41, 241
Draine, B. T., Roberge, W. G., & Dalgarno, A. 1983, ApJ, 264, 485
Dubner, G., Giacani, E., Reynoso, E., & Parón, S. 2004, A&A, 426, 201
Dubner, G. M., Moffett, D. A., Goss, W. M., & Winkler, P. F. 1993, AJ, 105, 2251
Falgarone, E., Verstraete, L., Pineau Des Forêts, G., & Hily-Blant, P. 2005, A&A, 433, 997
Frail, D. A., Goss, W. M., Reynoso, E. M., Giacani, E. B., Green, A. J., & Otrupcek, R. 1996, AJ, 111, 1651
Gry, C., Boulanger, F., Nehmé, C., Pineau des Forêts, G., Habart, E., & Falgarone, E. 2002, A&A, 391, 675
Harrus, I. M., & Slane, P. O. 1999, ApJ, 516, 811
Hartigan, P., Raymond, J., & Hartmann, L. 1987, ApJ, 316, 323
Hewitt, J. W., Yusef-Zadeh, F., & Wardle, M. 2008, ApJ, 693, 189
Hollenbach, D., & McKee, C. F. 1989, ApJ, 342, 306
Jones, A. P., Tielens, A. G. G. M., Hollenbach, D. J., & McKee, C. F. 1994, ApJ, 433, 797
Koralesky, B., Frail, D. A., Goss, W. M., Claussen, M. J., & Green, A. J. 1998, AJ, 116, 1323
Lazendic, J. S., Slane, P. O., Hughes, J. P., Chen, Y., & Dame, T. M. 2005, ApJ, 618, 733
Lazendic, J. S., Wardle, M., Whiteoak, J. B., Burton, M. G., & Green, A. J. 2004, arXiv:astro-ph/0409302
Le Bourlot, J., Pineau des Forêts, G., Flower, D. R., & Cabrit, S. 2002, MNRAS, 332, 985
McKee, C. F., Chernoff, D. F., & Hollenbach, D. J. 1984, Galactic and Extragalactic Infrared Spectroscopy, 108, 103
McKee, C. F., & Ostriker, J. P. 1977, ApJ, 218, 148
Moorhouse, A., Brand, P. W. J. L., Geballe, T. R., & Burton, M. G. 1991, MNRAS, 253, 662
Neufeld, D. A., Hollenbach, D. J., Kaufman, M. J., Snell, R. L., Melnick, G. J., Bergin, E. A., & Sonnentrucker, P. 2007, ApJ, 664, 890
Neufeld, D. A., et al. 2006, ApJ, 649, 816
Noriega-Crespo, A., Cotera, A., Young, E., & Chen, H. 2002, ApJ, 580, 959
Olbert, C. M., Keohane, J. W., Arnaud, K. A., Dyer, K. K., Reynolds, S. P., & Safi-Harb, S. 2003, ApJ, 592, L45
Pineau Des Forêts, G., & Flower, D. 2000, Molecular Hydrogen in Space, ed. F. Combes & G. Pineau des Forêts (Cambridge, UK: Cambridge Univ. Press), 117
Ramsbottom, C. A., Hudson, C. E., Norrington, P. H., & Scott, M. P. 2007, A&A, 475, 765
Reach, W. T., & Rho, J. 1999, ApJ, 511, 836
Reach, W. T., & Rho, J. 2000, ApJ, 544, 843

Reach, W. T., et al. 2006, AJ, 131, 1479
Reynoso, E. M., & Mangum, J. G. 2000, ApJ, 545, 874
Rho, J., Jarrett, T. H., Cutri, R. M., & Reach, W. T. 2001, ApJ, 547, 885
Rho, J., Kozasa, T., Reach, W. T., Smith, J. D., Rudnick, L., DeLaney, T., Ennis, J. A., & Gomez, H. 2008, ApJ, 673, 271
Richter, M. J., Graham, J. R., & Wright, G. S. 1995, ApJ, 454, 277
Savage, B. D., Bohlin, R. C., Drake, J. F., & Budich, W. 1977, ApJ, 216, 291
Slane, P., Chen, Y., Lazendic, J. S., & Hughes, J. P. 2002, ApJ, 580, 904
Smith, J. D. T., et al. 2007, ApJ, 656, 770
Tian, W. W., & Leahy, D. A. 2008, MNRAS, 391, L54
Timmermann, R. 1998, ApJ, 498, 246
Wilgenbus, D., Cabrit, S., Pineau des Forêts, G., & Flower, D. R. 2000, A&A, 356, 1010
Wilson, T. L. 1972, A&A, 19, 354
Yusef-Zadeh, F., Wardle, M., Rho, J., & Sakano, M. 2003, ApJ, 585, 319
Zhou, X., Chen, Y., Su, Y., & Yang, J. 2009, ApJ, 691, 516